Hindawi
International Journal of Aerospace Engineering
Volume 2021, Article ID 1781362, 10 pages
https://doi.org/10.1155/2021/1781362

Research Article

Effect of Reinforcement Fiber Arrangement on Thermal and Mechanical Properties of High Silica/Phenolic Resin Insulation Layer

Weihua Hui, Jinhang Wen, and XiaoMin Bu

Science and Technology on Combustion, Internal Flow and Thermo-Structure Laboratory, Northwestern Polytechnical University, Xi'an, Shaanxi 710072, China

Correspondence should be addressed to Weihua Hui; zhongyuancao@163.com

Received 9 August 2021; Revised 17 November 2021; Accepted 26 November 2021; Published 10 December 2021

Academic Editor: Kan Xie

The failure of the high silica/phenolic resin insulation layer under extreme thermal conditions has become an important reason for the trouble of solid rocket motors. A great number of studies have shown that the arrangement of reinforcement fibers is a significant factor in the failure of fiber-reinforced plastic. In this paper, the thermal and mechanical properties of the high silica/phenolic resin insulation layer with different arrangements were analyzed, and the causal relationship between the failure of the insulation layer and the arrangement of reinforcement fibers was given. Two types of heat-insulating layers with strong arrangement and weak arrangement were designed. After the SRM firing test, it is concluded that the essential reason for the failure of the insulation layer is the strength anisotropy caused by the weak arrangement of reinforcement fibers. Besides, the reinforcement fibers of strong arrangement are distributed in all directions, which compensates for the axial strength defects of the weakly arranged insulation layer.

1. Introduction

High silica glass fiber/phenolic resin composites have the characteristics of ablation resistance and good thermal insulation performance; thus, they are often used in the heat-insulating system of the tail-pipe nozzle. During the working process of a solid rocket motor (SRM), the insulation layer is always exposed to the combustion gas at high temperature and needs to be subjected to the severe ordeal of heat transfer and thermal stress. The design of the insulation layer directly affects the working reliability of the nozzle, which greatly influences the overall performance of the SRM [1–3]. Therefore, it is very important to analyze the failure mechanism and optimize the design of the SRM thermal insulation material.

Studying the heat exchange and temperature distribution of the high silica/phenolic resin insulation is the major approach to analyze the failure mechanism of the tail-pipe nozzle. The heat transmission of the nozzle is a complex process of coupling heat transfer of conduction, convection, and radiation. The actual temperature distribution is closely related to these factors, such as the structure of the nozzle and the material of the insulation layer. Many researchers have carried out a lot of researches on the thermal and mechanical properties of carbon fiber and high silica fiber-reinforced composites. Cecen et al. [4] conducted axial tensile, transverse tensile, bending, and short beam shear tests on unidirectional and biaxial carbon fibers reinforced with epoxy resin matrix composites. There is a significant difference in the ultimate tensile strength of the material that is parallel to the fiber arrangement direction and perpendicular to it, which fully proves the anisotropy of fiber-reinforced phenolic resin composites on the mechanical properties. Bartoli et al. [5] studied the mechanical properties of spherical and cylindrical rod-shaped carbon fiber-reinforced epoxy resin composites. The experimental results show that there is an obvious difference in the ultimate tensile strength and maximum elongation of epoxy resin composites with different carbon fiber microstructures, which confirms that the microstructure of reinforcement fibers has a significant

influence on the mechanical properties of the composite. Yao et al. [6] developed a method to improve the interface properties of composite materials by adjusting the fiber-matrix interphase structure and proved that the interlayer shear strength and bending strength of the composites significantly depend on the dispersion state and content of the carbon nanotubes in the interface region. Surendra Kumar et al. [7] compared the mechanical properties of composites at low temperature and normal temperature and studied the tensile and interlaminar shear failure mechanisms of carbon/epoxy composites at cryogenic temperature. Guo et al. [8] analyzed the stress-strain behavior of multiwalled carbon nanotubes/epoxy composites through tensile tests, using a scanning electron microscope (SEM), high-resolution transmission electron microscope, and X-ray diffraction to study the relationship between the microstructure and mechanical properties of the composites. Cui et al. [9] used the field emission scanning electron microscope (FE-SEM) to observe the microstructure and interfacial structure of the GF/Cu-Mo composite in the experiment, analyzed the distribution of elements by energy-dispersive spectroscopy (EDS) connected to the FE-SEM, and described the interfacial configuration and constitution of the composites using transmission electron microscopy. In conclusion, what it is mentioned above fully demonstrates that the arrangement of reinforcement fibers has great relation to the mechanical properties of materials. However, these researches are the results of mechanical tests under normal temperature and pressure conditions, which do not take into account that the high silica/phenolic resin insulation layer is in a harsh working environment of up to 3000 K in the actual working process. This problem needs to be solved urgently.

In order to study the performance changes of high silica/phenolic resins under high temperature environment, several methods have been developed to construct high temperature experimental environments. Patra et al. [10] utilized a platinum-rhodium furnace to heat the sample from normal temperature to 1250°C in nitrogen to simulate a high-temperature environment and adopted a combination of SEM and EDS to study the microstructure and thermal properties of ultrahigh-temperature ceramic-infiltrated carbon fiber composites at different temperatures. Kilic et al. [11] introduced the Nose-Hover thermostat to achieve temperature control, making it increase from 300 K to 900 K, and studied the energy, dynamic, thermal, and mechanical stability of TH-carbon. Torres-Herrador [12] developed a test methodology for determining the heat capacity and required heat of pyrolysis for carbon composites, which heated the carbon composite sample from normal temperature to 1100 K in an inert argon atmosphere by the platinum furnace. The heating devices commonly used at present can provide a high-temperature environment well and achieve precise temperature control. What should be pointed out is that these high-temperature test methods do not consider either that the insulation layer would be exposed to high temperature during the working process, or the high-speed continuous erosion to the insulation layer by the combustion gas at high temperature of about 3000 K.

All in all, the arrangement of reinforcement fibers has a great influence on the mechanical properties of the high silica/phenolic resin insulation layer. However, the actual working environment of the insulation layer evidently differs in these test methods. Therefore, the method of the solid rocket motor firing test must be adopted in order to accurately predict the thermal load of the insulation layer. This method not only is more consistent with the real working conditions but also makes detailed measurement and analysis of the pressure and temperature of the combustion chamber, the type of solid propellant, and combustion products. In order to correctly analyze the failure of the nozzle thermal insulation during operation, the microstructure of the thermal insulation layer composite material must be carefully observed so that researchers could summarize the characteristics of the microscopic arrangement of the fibers in the composite material and set up a comparison experiment by changing the microstructure method to research the effect of reinforcement fiber arrangements on the thermal and mechanical properties of composites. At present, this aspect has not gotten enough attention from scholars.

Two types of heat-insulating layer with strong arrangement and weak arrangement were designed, and SRM firing tests were carried out. It is shown that the main reason for the failure of the insulation layer is the weak arrangement of reinforcement fibers by the analysis comparative studies of the solid rocket motor firing test, SEM, and EDS.

2. Experiments

2.1. Insulation Layer Preparation. The thermal insulation layer of the nozzle was required to have both ablation resistance and good thermal insulation properties. Due to the long working time of more than ten seconds, the thermal protection layer is divided into two layers: the inner layer is an ablation resistant layer to resist thermal shock, chemical, and mechanical erosion, generally adopting carbon/phenolic, high silica/phenolic, and asbestos/phenolic to ensure that the size of the inner surface of nozzle, especially the size of the throat, remains unchanged; the outer layer is a heat insulation layer to reduce the heat transferred to the shell, usually using nitrile rubber filled with asbestos and silica fibers or high silica/phenolic and asbestos/phenolic. Considering the small size and short working time (about 2 seconds) of the SRM used in this paper, the thermal protection layer of the tail-pipe nozzle adopted a high silica/phenolic material, which serves as both ablation resistance and a heat insulation layer. Compared with resin composites reinforced by carbon and Kevlar reinforcement fibers, the advantages of this thermal protection scheme were low price, short production cycle, and no need for curing agents and catalysts in the curing and molding process.

In the process of chopped fiber molding, related parameters were determined according to the curing characteristics of the phenolic resin. More specifically, the viscous flow stage was 90°C to 110°C, the semicuring stage was 110°C to 130°C, and the hard curing stage is 130°C to 170°C. Firstly, the high silica reinforcement fibers of about 30 to 50 mm were premixed with the phenolic resin at 90°C to 110°C,

(a) (b)

Figure 1: The original photograph of high silica/phenolic resin: (a) weak arrangement and (b) strong arrangement.

and the mass ratio of the fibers to resin is 55 to 45. Then, the phenolic resin pressing and curing process must be experienced in the process of preparing high silica/phenolic resin composites. The pressing temperature is about 110°C, the heating rate is 30°C/h, the curing temperature is 165°C~180°C, and the curing time is 3 min~5 min/mm. As shown in Figure 1, different uniformities can be achieved by controlling the stirring time during the process of premixing reinforcement fibers and the resin, and the surface morphologies of the weak arrangement and the strong arrangement are very different. It is obvious that some fibers gathered into layered fiber bundles on the surface of the weak arrangement. On the contrary, fibers were arranged compactly and exhibit good uniformity after removing the oxide layer on the surface of the strong arrangement material.

2.2. Ground Firing Test System. In order to explore the influence of the arrangement of reinforcement fibers on the thermal and mechanical properties of the high silica/phenolic resin insulation layer, a solid rocket motor firing test was designed. The ground firing test system consists of experimental SRM, bench, data acquisition, ignition control, monitoring system, and other components, as shown in Figure 2. The experimental SRM was installed on the bench before the firing test, and the data acquisition module including pressure and thrust sensors and signal processors was used to obtain the pressure and thrust during work. The importance of the monitoring system was to record audio signals in dangerous environments accompanied by noise and high temperature, which could ensure the safety of testers. The engine started to work after the ignition control module sent a command, and the pressure, thrust, and audio data during engine operation were recorded for subsequent analysis. In addition, the nozzle assembly of SRM is shown in Figure 3. It was composed of a 30CrMnSiA shell, tungsten copper-infiltrated throat, and high silica/phenolic resin insulation layer. The thermal insulation layer was bonded on the inside of the shell. The internal burning star grain was used in the

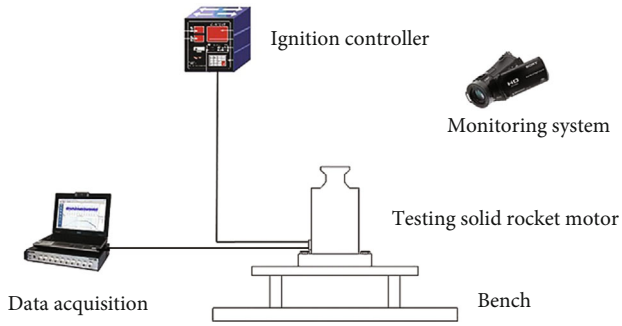

Figure 2: Ground firing test system.

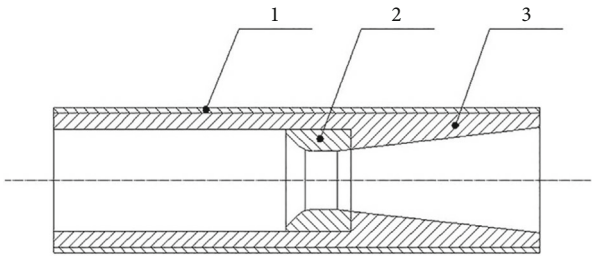

Figure 3: Schematic of the tail-pipe nozzle. 1: shell; 2: throat lining; 3: insulation layer.

solid rocket motor. The SRM was loaded with a composite propellant composed of 5 wt% aluminum powder and chemical fuel with assumed formula of $C_{9.5}H_{38.9}O_{24}N_6Cl_6$.

2.3. Test Project of Weak Arrangement. The thermal insulation layer used in the SRMα adopted the weak arrangement composites. Before the firing test, it is very necessary to observe the microstructure of the weak arrangement insulation layer to summarize the law of reinforcement fibers. The preparation process for SEM analysis cannot be ignored. First, we should determine the sampling location on the bulk raw material shown in Figure 1 and then obtain the surface with a large number of reinforcement fibers inside the

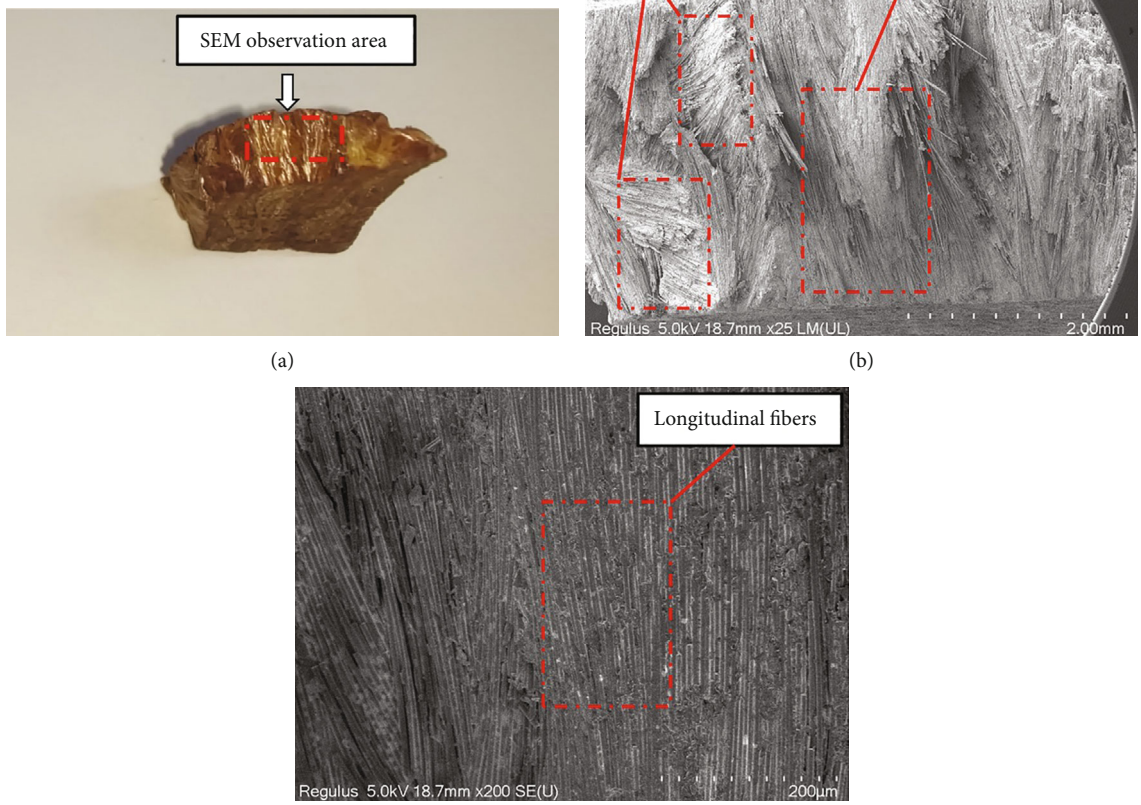

Figure 4: SEM microstructure of weak arrangement: (a) observation area, (b) 2.00 mm, and (c) 200 μm.

sample by breaking the outer resin, and finally vacuum coat the observation surface. To be specific, the Au wire was heated and evaporated by a large current in a vacuum environment and deposited on the surface of the sample. The thickness of the Au film is about 20-50 nm, which can not only reduce the damage of the electron beam to the sample but also increase the generation rate of the secondary electron and obtain good quality images.

The SEM observation area is shown in Figure 4(a), and the reinforcement fibers and phenolic resin matrix inside the composites can be directly observed. From the observation results of the insulation layer in Figures 4(b) and 4(c), it can be clearly seen that a large number of reinforcement fibers were distributed along the transverse and longitudinal directions in the observation area. However, there was a lack of reinforcement fibers that penetrate the plane of the observation area. According to the above rules, the yellow and green slender cylinders were used to represent the transverse and longitudinal fibers in the schematic diagram of Figure 5, which can clearly and accurately characterize the arrangement of reinforcement fibers in the weak arrangement heat-insulating layer, and can predict the strength defects in the direction perpendicular to the observation plane.

2.4. Improved Test Project of Strong Arrangement. The control experiment using the strong arrangement insulation

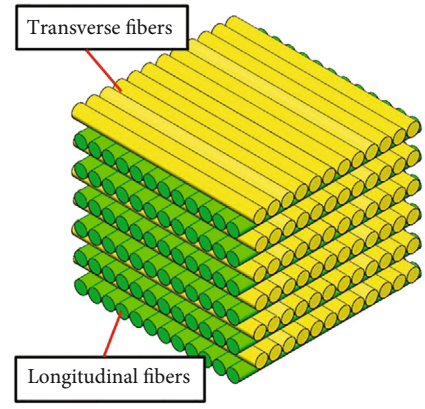

Figure 5: Schematic of weak arrangement.

layer was designed to solve the strength defects caused by inhomogeneous arrangement of reinforcement fibers. As mentioned in Section 2.1, the mixture must be fully stirred to mix the reinforcing fibers and the resin well during the preparation of the premix to ensure the uniformity of high silica fibers in all directions. Moreover, it is necessary to put up control experiments as much as possible to verify the effectiveness of the improvement. The improved SRMβ adopted strong arrangement high silica/phenolic resin composites produced as the thermal insulation layer, and other

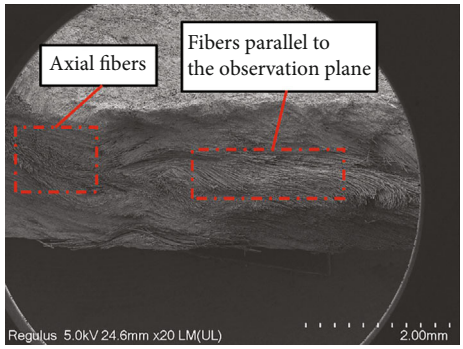

Figure 6: SEM microstructure of strong arrangement.

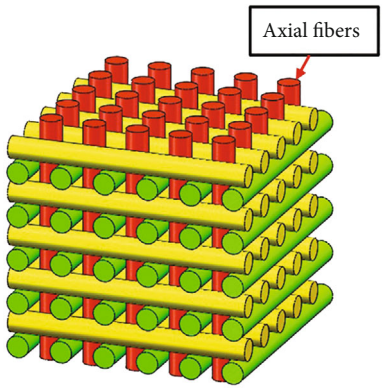

Figure 7: Schematic of strong arrangement.

design parameters of SRMβ were consistent with SRMα. The SEM microstructure observation was performed on the strong arrangement insulation before the firing test. As shown in Figure 6, there are a large number of reinforcing fibers parallel to the observation plane, and many axial fibers perpendicular to the observation plane cannot be ignored, which has formed a sharp contrast with the weak arrangement test in Figure 4. According to the above, regular, slender cylinders arranged in the axial, radial, and circumferential directions were used to represent reinforcement fibers in the strong arrangement heat-insulating layer in Figure 7, which means the reinforcement fibers were uniformly distributed in all directions, and there was no obvious strength defect.

3. Results and Discussion

3.1. Results of Weak Arrangement. Experiment data are shown in Figure 8. The ignition duration was 1.79 s, SRM work time was 1.12 s, the maximum pressure was 10.26 MPa, and the average pressure was 7.73 MPa. It is noticeable that the ignition pressure curve was normal without any abnormal fluctuations and the structure of the test SRM was complete. In order to study the structural change of the heat-insulating layer during the working process, the tail-pipe nozzle of the test SRMα was cut along the axis, as shown in Figure 9. The following details can be observed: (1) The ablation of the insulation layer was roughly uniform, and there was still a certain amount of ablation margin after

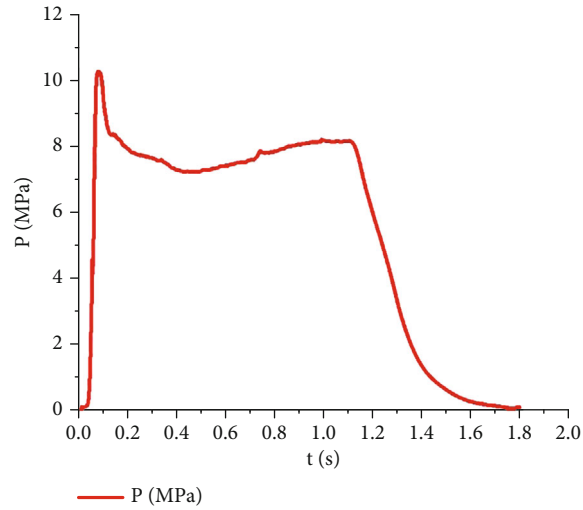

Figure 8: Ignition pressure curve.

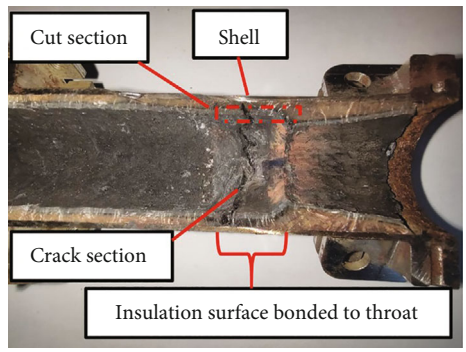

Figure 9: Sectional view of tail-pipe nozzle.

experiment; (2) After removing the tungsten copper-infiltrated throat, it can be clearly observed that there were annular cracks appearing in the weakly arranged insulation layer. And the corresponding 30CrMnSiA shell had a complete structure without any structural failure. (3) The axial distance between annular cracks and the front face of throat was about 4 mm, and the width of crack was about 1 mm. The microscopic surface of the crack was shown in Figure 10. And it is clear that some small cracks of different sizes can be seen scattered around the large cracks. Obviously, both the large cracks and the small ones presented the same tearing microstructural features that resin matrix on both sides of the crack had a tendency to expand along the axis of the nozzle. In addition, there were a small amount of shed fibers between the cracks, and there were no evident signs of mechanical damage near the crack area.

3.2. Analysis of Weak Arrangement Test Results

3.2.1. Analysis of Sediment. In this chapter, the chemical compositions of combustion products were calculated, and the energy-dispersive spectrometer (EDS) results of the insulation layer before and after the experiment were compared to analyze the elements change during the working process of the SRMα, which will provide a scientific basis to infer the failure mechanism of the heat-insulating layer. In this

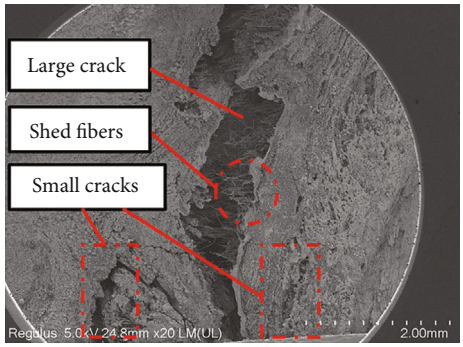

Figure 10: Insulation crack.

Table 1: Compositions of combustion products in the combustion chamber.

Species	Mole fraction (%)
CO (g)	27.461
H_2 (g)	25.791
H_2O (g)	19.413
HCl (g)	14.630
N_2 (g)	7.482
CO_2 (g)	3.139
Al_2O_3 (g)	2.084

paper, the equilibrium compositions of the propellant combustion products were calculated by the Chemical Equilibrium with Application Code, which is a free software for calculating chemical equilibrium products based on the free-energy-minimization principle. The estimated chamber pressure (7.73 MPa) was used to calculate the chemical equilibrium state. The calculation results show that the combustion products in the combustion chamber were composed of different types, as shown in Table 1. An energy-dispersive spectrometer was used to qualitatively and quantitatively analyze the element distribution in the microscopic area of the insulation layer. The EDS micrographs of the insulation layer are shown in Figure 11, and the EDS results of the weak arrangement insulation layer before and after the firing test are shown in Tables 2 and 3.

It can be found that the C content was significantly reduced by 22.48 percent and the Si content was obviously increased by 16.43 percent when comparing the EDS analysis results of the insulation surface bonded to the throat before and after the experiment. In particular, there was a slight increase by 0.52 percent in the Al content on the insulation surface bonded to the throat. Moreover, the results show that the Al elements inside the crack of the insulation layer also had no apparent change compared with the raw material before the experiment as shown in Table 3. According to the thermal insulating mechanism of the high silica/phenolic resin composites [13, 14], the phenolic resin of the insulation layer began to pyrolyze and decompose into low molecular hydrocarbons and gases difficult to ignite when the pyrolysis temperature of the resin was reached. As the temperature further rose, the stable carbonized layer was formed, and the reinforcement fibers inside the heat-insulating layer were exposed. The main component of the high silica fibers was SiO_2 while C was an important element of resin, which causes significant changes of the C and Si after the test.

In addition, the throat and the thermal insulation layer were bonded with epoxy resin adhesive in the production of the nozzle. There was an apparent discrepancy in the thickness between the carbonized layer on the surface bonded to the throat and the area directly affected by a large amount of combustion gas, as shown in the sectional view of the nozzle (Figure 9), which was due to the main heat for the insulation bonded to the throat coming from the conduction of the throat and the insulation not experiencing long-term scouring of high-temperature gas. Moreover, the epoxy resin adhesive between the throat and the insulation will experience the process of scouring because of the nozzle structure. With a small amount of gas entering the back side of the throat, the Al_2O_3 carried by the gas was attached to the insulation layer, which slightly increases the Al content of the insulation surface bonded to the throat after the test. Combined with the pressure curve and the microstructure of the insulation layer, the following details are considered: (1) the crack of the insulation layer did not cause abnormal fluctuations in the pressure curve; (2) the metal shell structure corresponding to the crack area is complete, and no serious ablation marks are found on the shell; and (3) the thermal insulation layer still has enough ablation margin after the experiment. It is fully proven that the crack section of the insulation layer has not been scoured for a long time by combustion gas, and the heat-insulating layer failure occurs after the ignition duration time, which can exclude the possibility of the crack being caused by the unqualified ablation properties.

3.2.2. Analysis of Crack. In the previous section, the qualitative and quantitative analyses for the element distribution in the microscopic area of the heat-insulating layer was carried out, and it was concluded that the failure of the insulation layer occurred after the end of the SRM work. After the solid rocket motor ground firing test, the nozzle was still in a high temperature environment for a long time after the propellant combustion was completed and the components of the tail-pipe nozzle were heated and expanded. Therefore, there were still great axial and radial thermal stresses inside the insulation layer. The thermal stress cannot be effectively transferred once there were defects inside the insulation layer, which will cause the insulation layer to fail and be destroyed. In order to further study the failure mechanism of the thermal insulation layer, the arrangement of reinforcement fibers was observed by scanning electron microscope.

In the sectional view of the tail-pipe nozzle (Figure 9), the cracks caused by the failure of the heat-insulating layer were called the crack section. Then, the nozzle assembly was cut along the symmetry axis to form the cut section. In order to fully and clearly observe the microstructure of the high silica/phenolic resin composites around the cracks, the observation method was to select a lower magnification to inspect the macroscopic characteristics of the sample

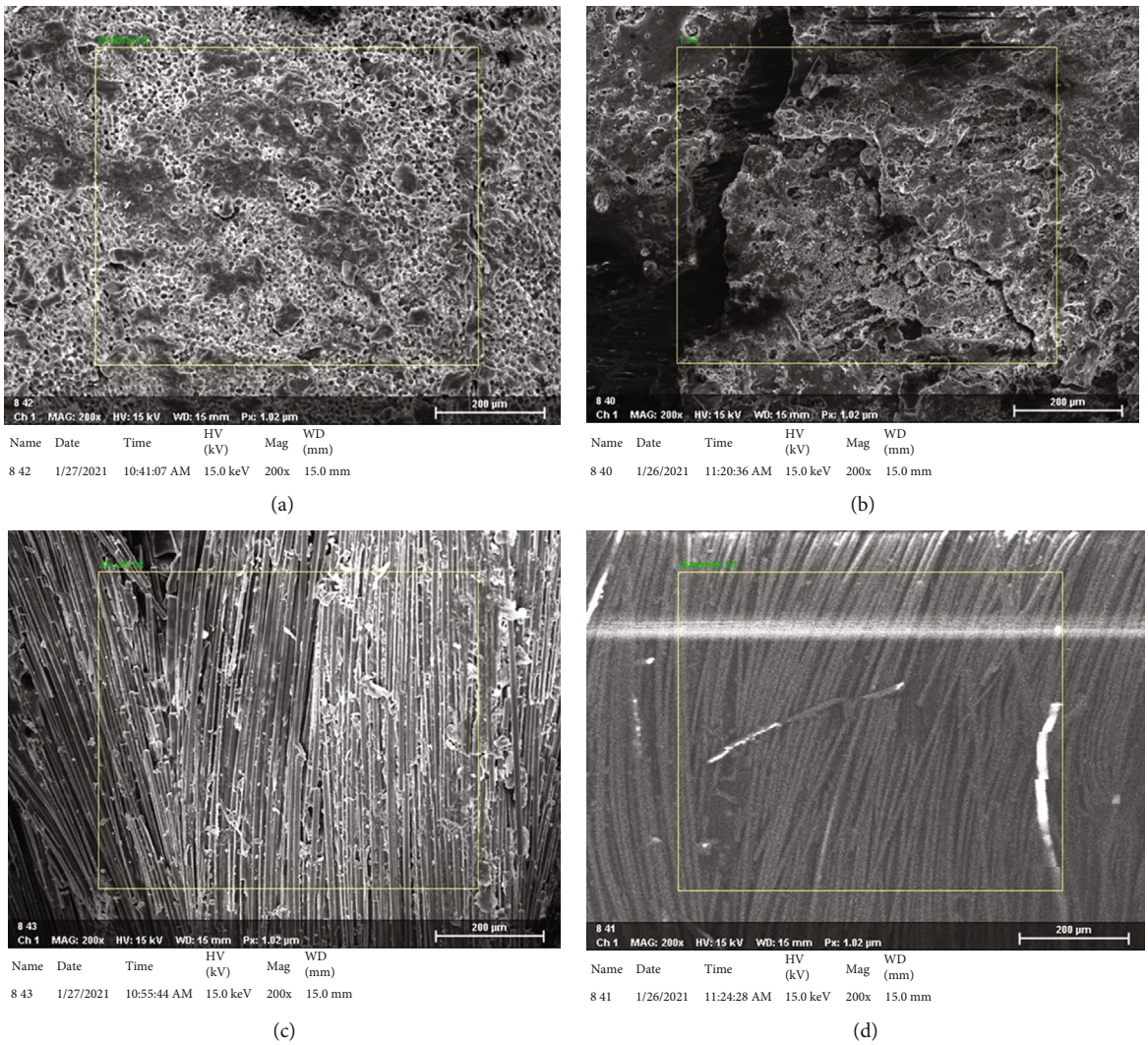

Figure 11: EDS micrograph of the insulation layer: (a) the surface bonded to the throat before the test, (b) the surface bonded to throat after the test, (c) the crack before the test, and (d) the crack after the test.

Table 2: EDS results of the surface bonded to the throat.

Species	Before the test (%)	After the test (%)	Change value (%)
C	53.41	30.93	-22.48
O	34.01	39.03	+5.02
Si	11.08	27.51	+16.43
Al	0.57	1.09	+0.52
Mg	0.31	0.61	+0.3
Na	0.63	0.82	+0.19

Table 3: EDS results of the crack.

Species	Before the test (%)	After the test (%)	Change value (%)
C	53.16	31.99	-21.17
O	20.84	44.92	+24.08
Si	24.36	22.46	-1.9
Al	0.48	0.37	-0.11
Mg	0.39	0.27	-0.12
Na	0.76	0	-0.76

and then gradually obtain greater magnification to achieve the information about direction of reinforcement fibers. As far as the observation angle was concerned, we look at the cut section of the crack and carefully record the characteristic information. Then, we break the insulation layer along the failed crack and observe the microstructure with attention concentrated on the crack section. Plenty of fibers that vertically penetrate to the cut section can be seen on the left side of Figure 12(a). At the same time, their circular cross-section can also be found on the right side of Figure 12(b), which shows that there are lots of circumferential fibers in the thermal insulation layer. It is clear that some fibers on the cut section were distributed perpendicular to the axis of SRM, and those gaps among them were filled by resin matrix material in Figure 13, which illustrates that there were abundant radial fibers in the cylindrical heat-insulating layer. What should be noted was that high silica fibers distributed along the axial direction of the nozzle were

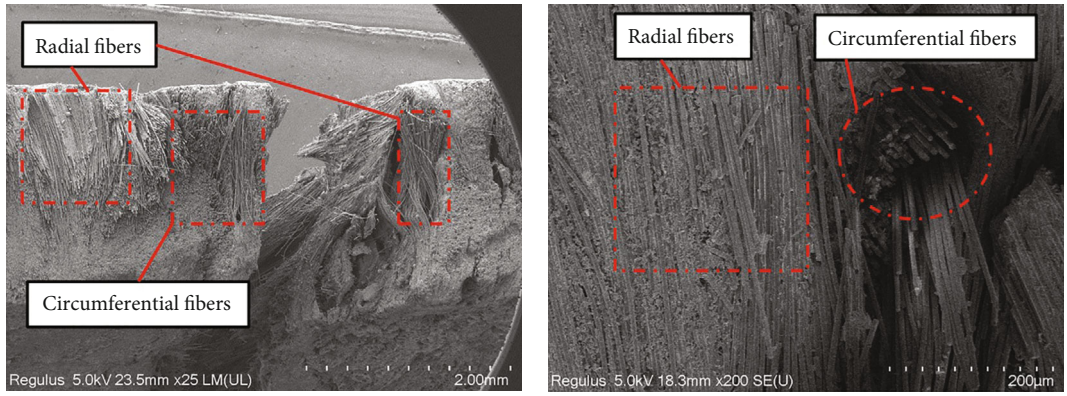

(a) (b)

Figure 12: SEM of the cut section: (a) 2.00 mm and (b) 200 μm.

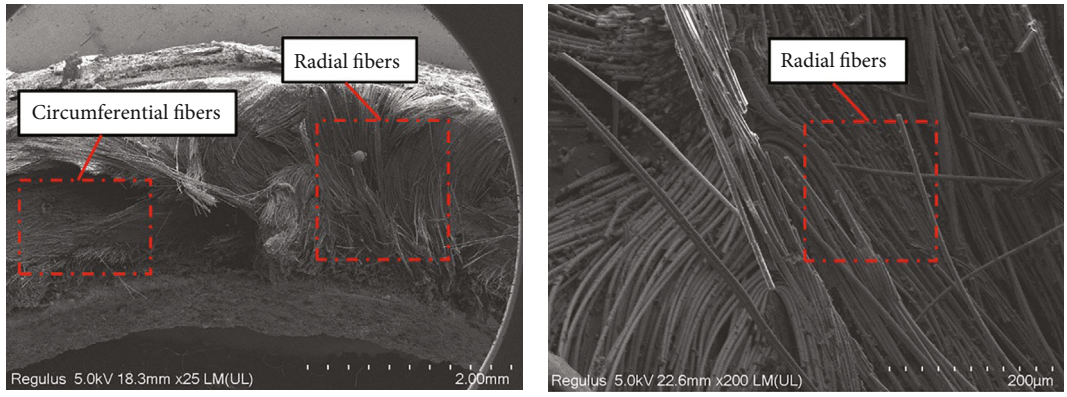

(a) (b)

Figure 13: SEM of the crack section: (a) 2.00 mm and (b) 200 μm.

not observed in both the cut section and the crack section. After summarizing the SEM analysis results, we can find that the weak arrangement insulation layer used in SRMα has large quantities of circumferential and radial fibers, but lacks reinforcement fibers distributed along the axial direction of the nozzle.

3.3. Results of Strong Arrangement. According to the principle of the control experiment, the ground firing test of the improved SRMβ was carried out under the same external condition, such as atmospheric pressure and temperature. The pressure curves of the two experiments were almost identical, so the pressure curve of SRMβ was not given. The test results showed that the ignition process of SRMβ was normal and the appearance structure of the metal shell was complete. The tail-pipe nozzle of the improved SRMβ was also cut along the axial direction same as the original experimental procedure, as shown in Figure 14. The structure of the high silica/phenolic resin insulation layer produced by short fiber compression molding was complete without any destructive crack. It is distinct from the testing project that the strong arrangement effectively makes up for the defects of the weak arrangement, and the thermal and mechanical properties of the insulation layer had been significantly improved.

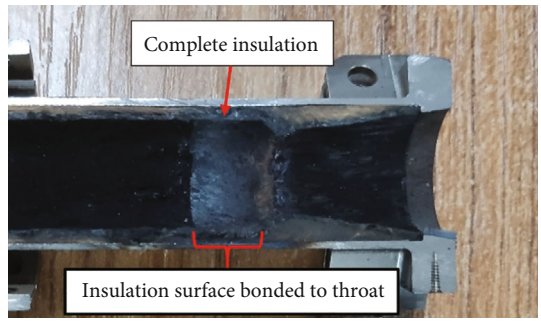

Figure 14: Sectional view of improved tail-pipe nozzle.

3.4. Comparison for Two Types of Heat-Insulating Layer. In order to study the effect of the enhanced fiber arrangement on the thermal and mechanical properties of high silica/phenolic resin composites, two types of heat-insulating layers with different arrangements for reinforcement fibers were designed in this paper. Combining the results of comparative experiments to summarize the previous SEM and EDS results, these two types of insulation have the following differences:

(1) *Arrangement of reinforcement fibers.* The weak arrangement insulation layer used for SRMα has

Table 4: Performance of high silica/phenolic composites.

Properties	Testing direction	Weak arrangement	Strong arrangement
Tensile strength (MPa)	Parallel	82.7	61.9
	Vertical	5.0	
Tensile modulus $\times 10^{-3}$ (MPa)	Parallel	18.1	31.7
	Vertical	3.31	

large quantities of circumferential and radial fibers, but lacks reinforcement fibers distributed along the axial direction of the nozzle. In contrast, the strong arrangement fibers were uniformly distributed in each direction.

(2) *Tensile strength*. As shown in Table 4, there was a huge difference in tensile strength between the parallel direction where the reinforcement fibers were laid and the vertical direction where the fibers were missing. And the tensile strength of the parallel layer was significantly better. Judging from the structural characteristics of high silica fiber phenolic resin composites, there were a great number of short fibers in the thermal insulation layer produced by the chopped fiber molding. The ability to bear the load was limited to the axial direction of the long fiber, while the radial strength mainly depended on the cohesive strength of the phenolic resin. There is no doubt that the tensile strength of high silica fibers is greatly different from phenolic resin, which is the main reason for the anisotropy of the thermal and mechanical properties. It should be noted that the reinforcing fibers and the resin matrix will not be uniformly mixed if sufficient stirring is not experienced during the premixing process. As shown in Figure 1(a), the phenomenon that the fibers aggregate into bundles and are arranged in layers will be inevitable. Under the action of the external load, the defective material will be destroyed in the direction perpendicular to the fiber bundle. On the contrary, the reinforcement fibers are distributed in all directions if the premixing process is fully stirred, and the phenolic resin fills the gaps between the fibers. Therefore, the ability of strong arrangement materials to withstand loads in all directions is the same. In short, the strong arrangement insulation layer made up for the lack of axial strength and solved the problem of composite material performance anisotropy caused by the weak arrangement of reinforcement fibers.

4. Conclusions

Two types of heat insulation with different arrangements of reinforcement fibers were designed, and the SRM firing test was carried out to compare their thermal and mechanical properties. The element composition of the insulation layer and the arrangement of reinforcement fibers before and after the test were carefully studied through the method combining EDS and SEM. And the failure mechanism of the insulation layer was systematically analyzed. Based on the above experiment and analysis, the following conclusions are obtained:

(1) The arrangement of reinforcement fibers is a decisive factor for the thermal and mechanical properties of the high silica/phenolic resin composites. The weak arrangement insulation layer lacks reinforcement fibers distributed along the nozzle axis, which leads to axial strength defect and causes the insulation layer to be damaged during the actual application of the tail-pipe nozzle. And the reinforcement fibers of strong arrangement are distributed in all directions, which compensates for the axial strength defects of the weakly arranged insulation layer

(2) It is necessary to ensure the consistency of strength in every direction to avoid the failure caused by inappropriate arrangement of reinforcement fibers when the high silica fiber-reinforced plastics are used as the heat-insulating layer for the solid rocket motor

Data Availability

All the data used to support the findings of this study are available from the corresponding author upon request.

Conflicts of Interest

The authors declare that there is no conflict of interest regarding the publication of this paper.

References

[1] V. Borie, J. BRULARD, and G. Lengelle, "An aerothermochemical analysis of carbon-carbon nozzle regression in solid-propellant rocket motors," in *AIAA, ASME, SAE, and ASEE, Joint Propulsion Conference, 24th*, p. 13, Boston, MA; United States, 1988, 1988 July. https://www.proquest.com/conference-papers-proceedings/aerothermochemical-analysis-carbon-nozzle/docview/24925280/se-2?accountid=28284.

[2] K. K. Kuo and S. T. Keswani, "A comprehensive theoretical model for carbon-carbon composite nozzle recession," *Combustion Science and Technology*, vol. 42, no. 3-4, pp. 145–164, 1985, https://www.proquest.com/scholarly-journals/comprehensive-theoretical-model-carbon-composite/docview/24513679/se-2?accountid=28284.

[3] P. C. Gasson, "Book reviews: aerospace materials and material technologies. Vol. 1: aerospace materials," *The Aeronautical Journal*, vol. 122, no. 1251, pp. 849–853, 2018, https://www.proquest.com/scholarly-journals/book-reviews-aerospace-

materials-material/docview/2034168590/se-2?accountid=28284.

[4] V. Cecen, M. Sarikanat, H. Yildiz, and I. H. Tavman, "Comparison of mechanical properties of epoxy composites reinforced with stitched glass and carbon fabrics: characterization of mechanical anisotropy in composites and investigation on the interaction between fiber and epoxy matrix," *Polymer Composites*, vol. 29, no. 8, pp. 840–853, 2008, https://www.proquest.com/scholarly-journals/comparison-mechanical-properties-epoxy-composites/docview/33540325/se-2?accountid=28284 (accessed August 4, 2021).

[5] M. Bartoli, C. Rosso, M. Giorcelli et al., "Effect of incorporation of microstructured carbonized cellulose on surface and mechanical properties of epoxy composites," *Journal of Applied Polymer Science*, vol. 137, no. 27, p. 7, 2020, https://www.proquest.com/scholarly-journals/effect-incorporation-microstructured-carbonized/docview/2390480767/se-2?accountid=28284.

[6] H. Yao, X. Sui, Z. Zhao et al., "Optimization of interfacial microstructure and mechanical properties of carbon fiber/epoxy composites via carbon nanotube sizing," *Applied Surface Science*, vol. 347, no. 8, pp. 583–590, 2015, https://www.proquest.com/scholarly-journals/optimization-interfacial-microstructure/docview/1709736384/se-2?accountid=28284.

[7] M. Surendra Kumar, N. Sharma, and B. C. Ray, "Microstructural and mechanical aspects of carbon/epoxy composites at liquid nitrogen temperature," *Journal of Reinforced Plastics and Composites*, vol. 28, no. 16, pp. 2013–2023, 2009, https://www.proquest.com/scholarly-journals/microstructural-mechanical-aspects-carbon-epoxy/docview/34771533/se-2?accountid=28284.

[8] P. Guo, H. Song, and X. Chen, "Interfacial properties and microstructure of multiwalled carbon nanotubes/epoxy composites," *Materials Science and Engineering A: Structural Materials: Properties, Microstructures and Processing*, vol. 517, no. 1-2, pp. 17–23, 2009, https://www.proquest.com/scholarly-journals/interfacial-properties-microstructure-multiwalled/docview/34507125/se-2?accountid=28284.

[9] Q. Cui, C. Chen, Y. Chengwei et al., "Effect of molybdenum particles on thermal and mechanical properties of graphite flake/copper composites," *Carbon*, vol. 161, no. 5, p. 169, 2020, https://www.proquest.com/scholarly-journals/effect-molybdenum-particles-on-thermal-mechanical/docview/2441576598/se-2?accountid=28284.

[10] N. Patra, N. al Nasiri, D. D. Jayaseelan, and W. E. Lee, "Thermal properties of C_f/HfC and C_f/HfC-SiC composites prepared by precursor infiltration and pyrolysis," *Journal of the European Ceramic Society*, vol. 38, no. 5, pp. 2297–2303, 2018.

[11] M. E. Kilic and K.-R. Lee, "Tuning the electronic, mechanical, thermal, and optical properties of tetrahexcarbon via hydrogenation," *Carbon*, vol. 161, pp. 71–82, 2020.

[12] F. Torres-Herrador, A. Turchi, K. M. van Geem, J. Blondeau, and T. E. Magin, "Determination of heat capacity of carbon composites with application to carbon/phenolic ablators up to high temperatures," *Aerospace Science and Technology*, vol. 108, article 106375, 2021.

[13] S. Shi, C. Gong, J. Liang, G. Fang, L. Wen, and L. Gu, "Ablation mechanism and properties of silica fiber-reinforced composite upon oxyacetylene torch exposure," *Journal of Composite Materials*, vol. 50, no. 27, pp. 3853–3862, 2016.

[14] M. A. Mirzapour, H. R. Haghighat, and Z. Eslami, "Effect of zirconia on ablation mechanism of asbestos fiber/phenolic composites in oxyacetylene torch environment," *Ceramics International*, vol. 39, no. 8, pp. 9263–9272, 2013.